JMEPEG (2017) 26:1801–1807
DOI: 10.1007/s11665-017-2549-2

1059-9495/$19.00

Butt Welding of 2205/X65 Bimetallic Sheet and Study on the Inhomogeneity of the Properties of the Welded Joint

Ning-Nian Gou, Jian-Xun Zhang, Jian-Long Wang, and Zong-Yue Bi

(Submitted May 17, 2016; in revised form December 13, 2016; published online March 21, 2017)

The explosively welded 2205 duplex stainless steel/X65 pipe steel bimetallic sheets were butt jointed by multilayer and multi-pass welding (gas tungsten arc welding for the flyer and gas metal arc welding for the transition and parent layers of the bimetallic sheets). The microstructure and mechanical properties of the welded joint were investigated. The results showed that in the thickness direction, microstructure and mechanical properties of the welded joint exhibited obvious inhomogeneity. The microstructures of parent filler layers consisted of acicular ferrite, widmanstatten ferrite, and a small amount of blocky ferrite. The microstructure of the transition layer and flyer layer consisted of both austenite and ferrite structures; however, the transition layer of weld had a higher volume fraction of austenite. The results of the microhardness test showed that in both weld metal (WM) and heat-affected zone (HAZ) of the parent filler layers, the average hardness decreased with the increasing (from parent filler layer 1 to parent filler layer 3) welding heat input. The results of hardness test also indicated that the hardness of the WM and the HAZ for the flyer and transition layers was equivalent. The tensile test combined with Digital Specklegram Processing Technology demonstrated that the fracturing of the welded joint started at the HAZ of the flyer, and then the fracture grew toward the base metal of the parent flyer near the parent HAZ. The stratified impact test at −5 °C showed that the WM and HAZ of the flyer exhibited lower impact toughness, and the fracture mode was ductile and brittle mixed fracture.

Keywords bimetallic sheet butt welding, inhomogeneity, mechanical property, microstructure

1. Introduction

Bimetallic sheets can take full advantages of the two materials at a lower cost, to achieve the performance that cannot be provided by a single metal such as high strength, well wear resistance, and excellent corrosion resistance (Ref 1). Explosive welding is one of the most widely used methods capable of producing a wide variety of both similar and dissimilar bimetallic sheets such as stainless steel/steel (Ref 2), aluminum/aluminum (Ref 3), steel/titanium alloy (Ref 4-6), aluminum/copper (Ref 7), and titanium alloy/copper (Ref 8).

The prospect of bimetallic sheets is promising, and the welding of the bimetallic sheets is the key factor in its application. However, due to the obvious difference of the properties between the layer and parent metal of the bimetallic sheets, welding of the bimetallic sheets encounters some difficulties, such as low welding efficiency and complex welding process (Ref 9, 10). This usually leads to complex microstructure and inferior properties of the welded joint. In this study, explosively welded 2205 duplex stainless steel/X65 pipe steel (2205/X65) bimetallic sheet was butt jointed by multilayer and multi-pass welding. Furthermore, the microstructure and mechanical properties of the welded joint were studied through optical microscopy, microhardness test, tensile test, and the Charpy V-notch impact test. The main objective of this study was to present a typical case of the inhomogeneity of the structure and the mechanical properties of the butt-welded joint for the bimetallic sheets. It was also necessary to obtain causes of the occurrence of this inhomogeneity in order to give some reference to the technical staffs who are involved in the welding engineering of bimetallic sheets.

2. Materials and Methods

The material employed for this investigation was the explosively welded 2205/X65 bimetallic sheet with 18 mm thickness (including flyer layer with 2 mm thickness and parent layer with 16 mm thickness). Figure 1(a) displays the groove dimensions of the bimetallic sheets. Figure 1(b) exhibits the schematic illustration of the welding procedure. The flyer layers were joined together by a single-pass gas tungsten arc welding, and the filler wires were AWS A5.9 ER2209. The parent layers were joined together by multilayer and multi-pass gas metal arc welding (GMAW), and the filler wires were ER55-1. Another GMAW pass with the same filler wire (AWS A5.9 ER2209) was carried out between flyer layer fusion zone (FZ) and parent layer FZ as a transition layer. Table 1 lists the chemical composition of the bimetallic sheets and filler wire. Table 2 lists the welding process parameters.

To investigate the microstructure in each zone of the welded joint, samples were cut from the weldment and prepared by conventional metallographic methods involving grinding, polishing, and etching. The parent layer of the welded joint was

Ning-Nian Gou, Jian-Xun Zhang, and **Jian-Long Wang**, State Key Laboratory of Mechanical Behavior for Materials, Xi'an Jiaotong University, Xi'an 710049, China; and **Zong-Yue Bi**, Baoji Petroleum Steel Pipe Co., Ltd., Baoji 721008 Shanxi, China. Contact e-mail: jxzhang@mail.xjtu.edu.cn.

etched in 4% Nital, and the flyer layer and transition layer of the welded joint were etched in a solution containing alcohol (100 mL), HCl (100 mL), and $CuCl_2$ (5 g). The microstructural features were then examined using a Nikon Eclipse MA200 type optical microscope. Figure 2 depicts the optical microscopy images of the welded joint, clearly indicating that the joint obtained was free of defects. The bonding lines of the multilayer welds are clearly visible under low magnification, as exhibited in Fig. 2. Microhardness measurements were taken by using a Vickers hardness tester with a load of 100 g for 10-s dwell time. The test areas consisted of the base materials (BMs), heat-affected zones (HAZs), and weld metal (WM) in each layer of the joint. A tensile test was performed for the welded joint. During the tensile testing, the strain distribution in the welded joint was measured at a speed of 2 frames per second by Digital Specklegram Processing Technology. The tensile specimens were fabricated with the dimensions shown in Fig. 3.

In order to evaluate the toughness of the joint, a stratified impact test was performed. The stratified specimens were collected using the method shown in Fig. 4, and the impact test specimens with 55 mm × 10 mm × 5 mm dimensions were cut from the stratified specimens. The notch face of the impact test specimens that was parallel to the cross section of the welded joint, and the notch which was parallel to the thickness direction of the weldment were located in the WM and in the HAZ, respectively. The tests were

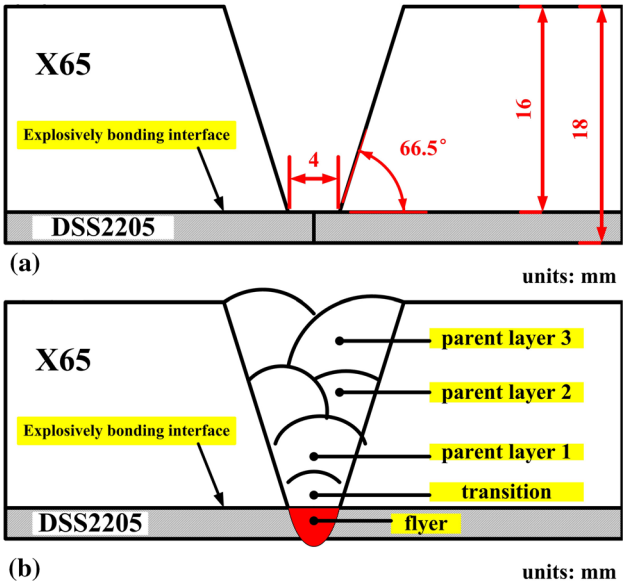

Fig. 1 Schematic illustration of the groove dimensions and welding procedure

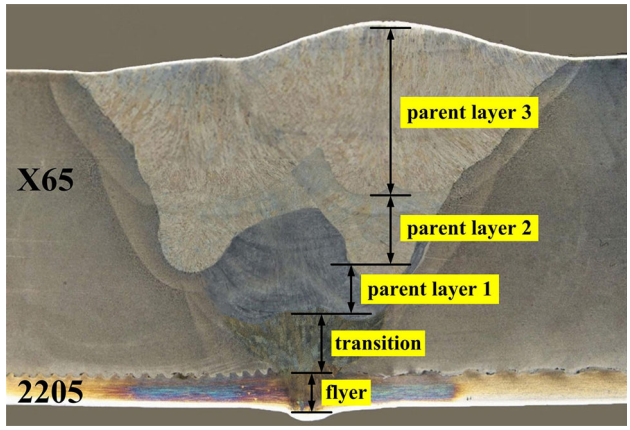

Fig. 2 Morphology of the cross section of the welded joint

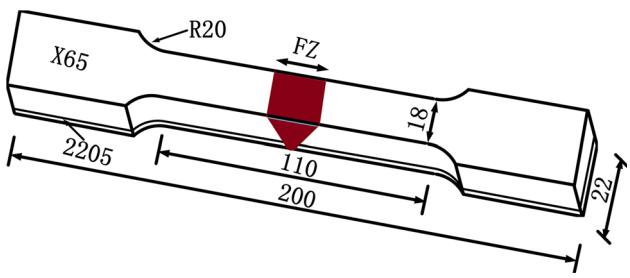

Fig. 3 Dimensions of the tensile specimen (unit: mm)

Table 1 Chemical compositions of materials employed (wt.%)

Materials	C	Si	Mn	P	S	Cr	Ni	Mo	N	Fe
2205	≤ 0.030	≤ 1.00	2.00	≤ 0.030	≤ 0.020	22.0–23.0	4.5–6.5	3.0–3.5	0.14–0.20	Balance
X65	0.046	0.24	1.6	0.099	0.017	0.042	0.016	0.16	0.15	Balance
ER2209 (Ø1.2 mm)	≤ 0.03	≤ 0.90	0.5–2.0	≤ 0.03	≤ 0.02	21.5–23.5	7.5–9.5	2.5–3.5	0.08–0.20	Balance
ER55-1 (Ø1.2 mm)	≤ 0.1	0.6	1.2–1.6	≤ 0.03	≤ 0.03	0.3–0.9	0.2–0.6	…	…	Balance

Table 2 Welding process parameters and the heat inputs

Layer	Pass	Current, A	Volt, V	Speed, cm min^{-1}	Gas	Gas, L min^{-1}	Heat input, kJ cm^{-1}
Flyer	1	145	12.5	30	Ar + 3%N_2	10	3.625
Transition	1	156	19.5	30	Ar + 3%N_2	18	6.084
Parent layer 1	1	156	19.3	30	Ar + 2%CO_2	18	6.084
Parent layer 2	2	235	21.1	30	Ar + 2%CO_2	18	9.917
Parent layer 3	2	271	27.2	30	Ar + 2%CO_2	18	14.742

performed at −5 °C, and three specimens were tested at each position. After impact test, the fracture was examined using a LS-JLLH-22 scanning electron microscope, and the fracture characteristics of the joint were analyzed by combining the metallographic examination consequences.

3. Results and Discussion

3.1 Microstructure Characterization

Higher magnification micrographs of the welded joint are displayed in Fig. 5 and 6. Figure 5 reveals the microstructures in three parent filler layers and the corresponding HAZ of the welded joint. Figure 5(a) and (c) shows the microstructures in the WM of the parent filler layers 1 and 2. Figure 5(a) and (c) shows that the original austenite grain boundary is clearly visible. In original intracrystalline austenite, a large amount of acicular ferrite is generated which constitutes the main metallographic structure of the WM; in the original austenite grain boundary, a continuous sheet of larger westergren ferrite is generated. A vast body of research shows that widmanstatten structure, and inclusion and banded structure in WM are main reasons responsible for a decrease in the impact property (Ref 11, 12). Figure 5(e) shows the microstructures in the WM of the parent filler layer 3, revealing that its metallographic structure mainly consists of acicular ferrites staggered on each other. Owing to the existence of a large number of dislocations, this metallographic structure is beneficial to improve the toughness of WM. Figure 5(b) exhibits that the microstructure of HAZ consists of granular bainite and bainitic ferrite. With the increase in heat input on the parent filler layer 2, change in the microstructure was not observed; however, its grain size became more uneven as demonstrated in Fig. 5(d). Further, Fig. 5(f) shows the microstructures in the HAZ of the parent filler layer 3. The figure clearly exhibits that the main microstructure of the HAZ mainly consists of large polygonal ferrite and acicular ferrite, and the grain size of the ferrite reaches 20 μm in addition to a small amount of acicular ferrite. This phenomenon could be attributed to the extremely low cooling speed caused by the largest heat input (Ref 12).

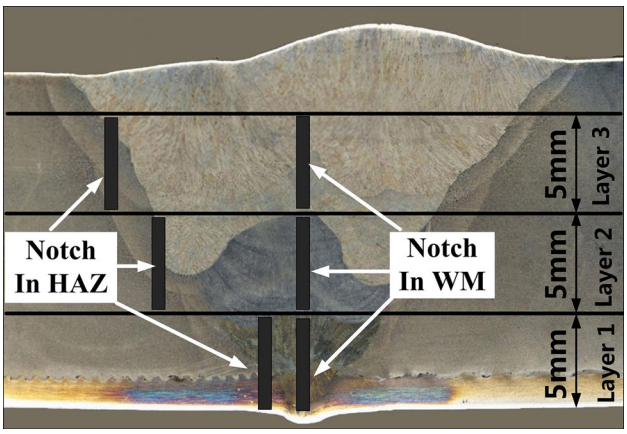

Fig. 4 Stratified scheme for stratified Charpy V-notch impact test for welded joint

Figure 6 clearly illustrates the microstructural evolution in the transition layer and flyer layer of the welded joint. Figure 6(a) shows that the microstructure of the flyer layer FZ consists of networks of austenite (A) at ferrite grain

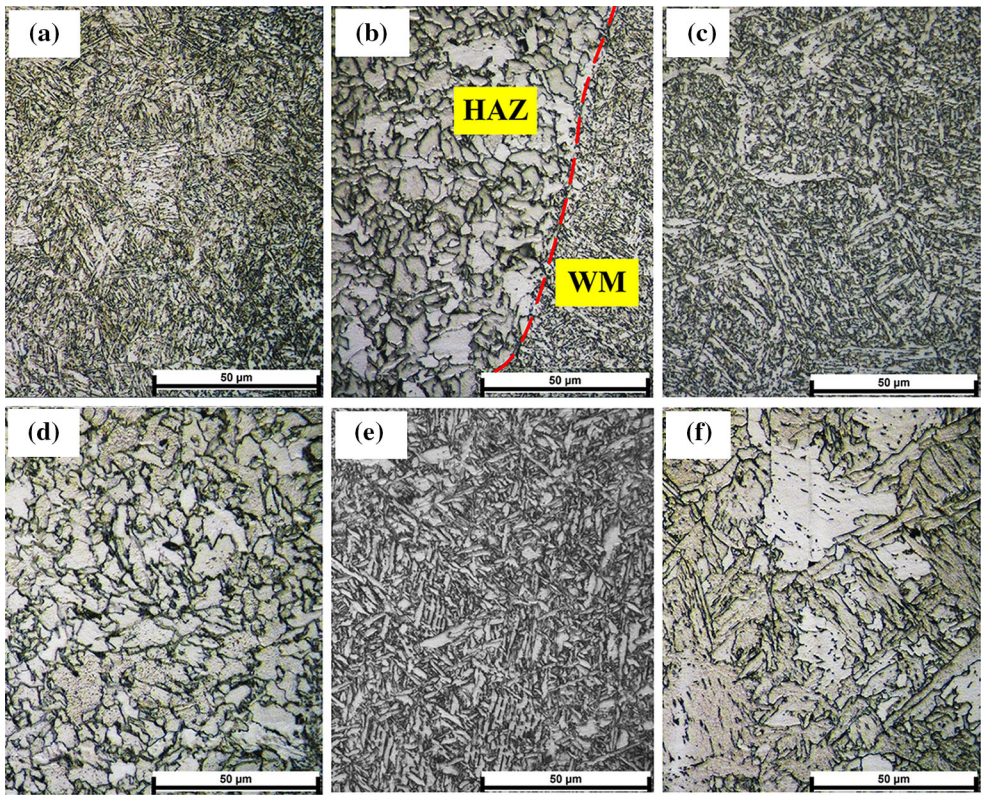

Fig. 5 Optical microscopy images of the cross section of the welded joint

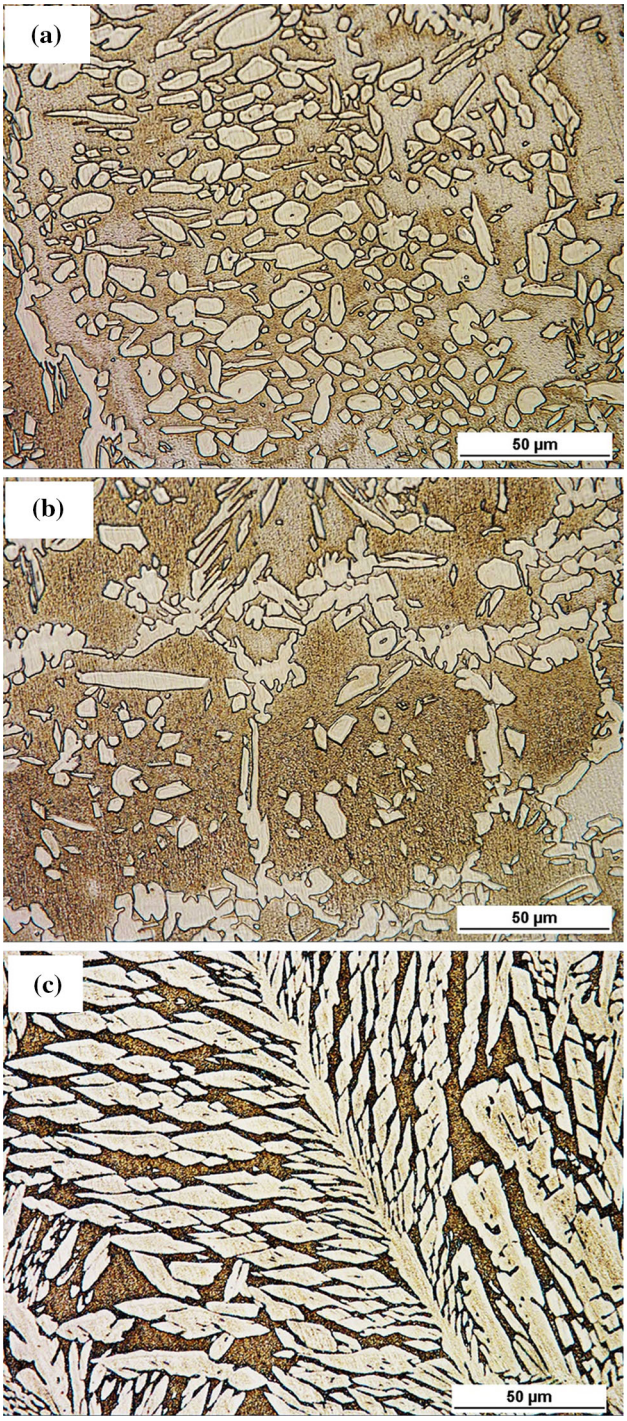

Fig. 6 Optical microscopy images of the welded joint

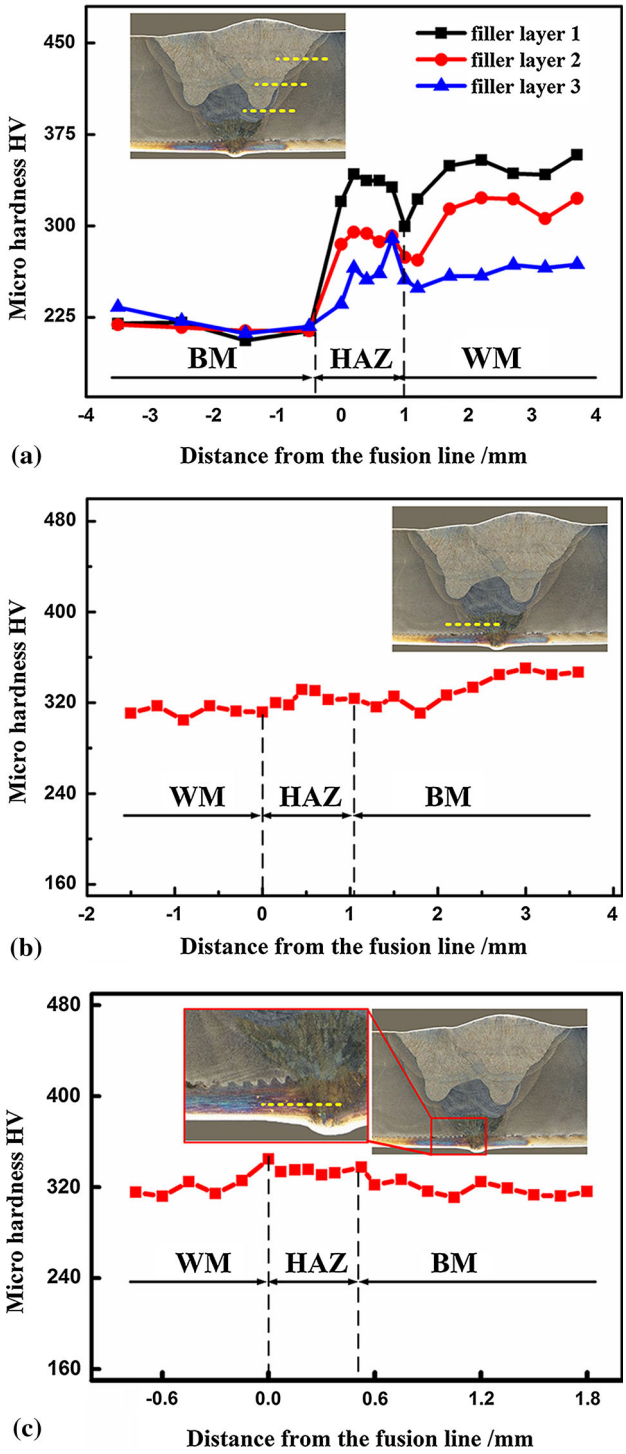

Fig. 7 Results of the microhardness profile on the cross section

boundaries and is land-like austenite (A) precipitates embedded in the continuous ferrite (F). Figure 6(b) shows the microstructural features of the flyer layer HAZ. In this zone, depending on the thermal cycles of the welding process, the original ferrite/austenite balance was disturbed, and austenite was present as grain boundary allotriomorphs along the ferrite grain boundaries. Statistics showed that the volume fraction of austenite in the flyer layer HAZ was 38% which is acceptable for the most industrial applications (Ref 11). Figure 6(a) shows that the microstructure of the transition layer FZ consists of both austenite and ferrite structures. Clearly, the austenite is distributed as intensive island formed in the continuous ferrite (F), statistics showed that the austenite content was as high as 70%, and this could be attributed to the increase in the heat input (see Table 2).

3.2 Mechanical Properties

3.2.1 Microhardness Profile. Figure 7 shows the results of the microhardness test on the cross section of the welded joint. The microhardness measurement paths are shown in the

insets in Fig. 7(a), (c), and (d). Figure 7(a) shows the microhardness distribution of parent filler layers. Clearly, the WM in each filler layer exhibits the highest hardness, HAZ shows low hardness, and BM shows the smallest value of hardness, which ranges from 210 to 225 HV. Figure 7(a) clearly demonstrates that in both WM and HAZ of the parent filler layers, the hardness gradually decreases according to the welding sequence of the filler layers. In other words, in both WM and HAZ of the parent filler layers, the average hardness decreased with the increasing (from parent filler layer 1 to parent filler layer 3) welding heat input. Figure 7(b) shows the microhardness distribution of transition layer, indicating that the microhardness increases from the WM to BM. The average hardness of WM (2209) was approximately 320 HV, and this was about 10 HV lower than that of HAZ. However, the average hardness in the BM (X65 near the explosively bonded interface) of transition layer was 330 HV which was significantly higher than that of the BM far away from the explosively bonded interface. This phenomenon could be attributed to the high plastic deformation in the explosive welding zone as reported by many researchers (Ref 2, 7). Figure 7(c) shows the microhardness distribution of filler layer. Apparently, the WM and BM (2205) share the same average hardness values corresponding to about 320 HV. However, the HAZ shows little

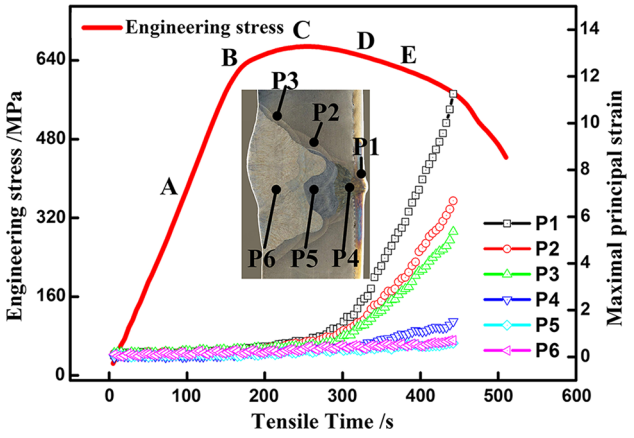

Fig. 8 Stress-time curves of the tensile test for the joint and the change in the maximum principal strain over time at positions 1–6 as described in the inset

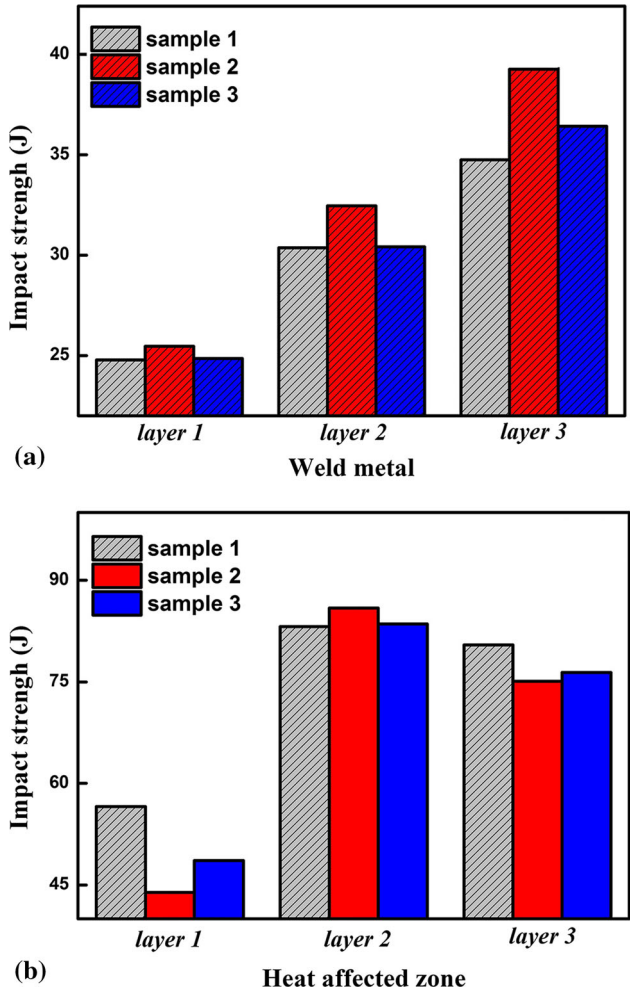

Fig. 10 Stratified Charpy V-notch impact test results for the welded joint constructed at −5 °C: (a) weld metal and (b) HAZ

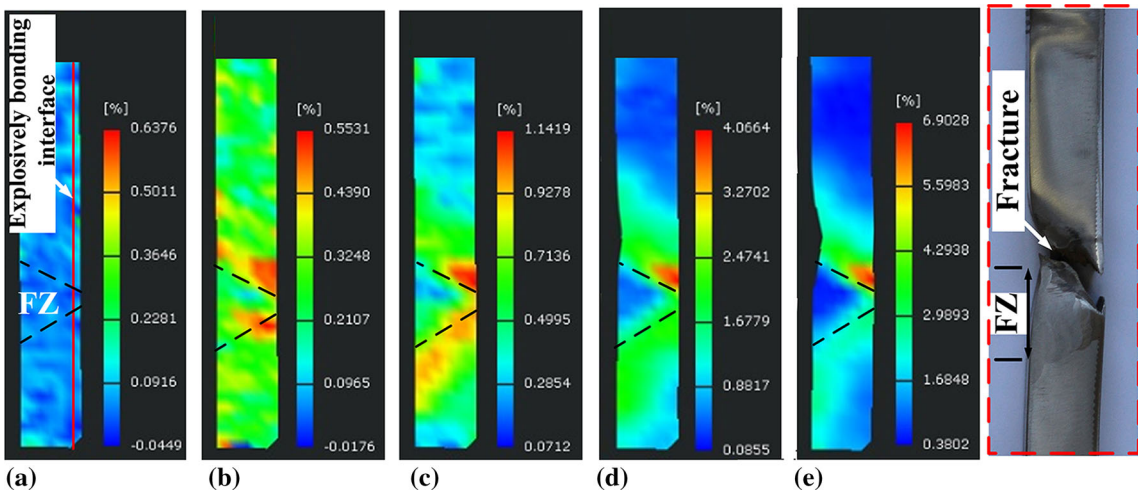

Fig. 9 Corresponding localized strain distributions on the surface for the same tensile specimen at points A, B, C, D, and E

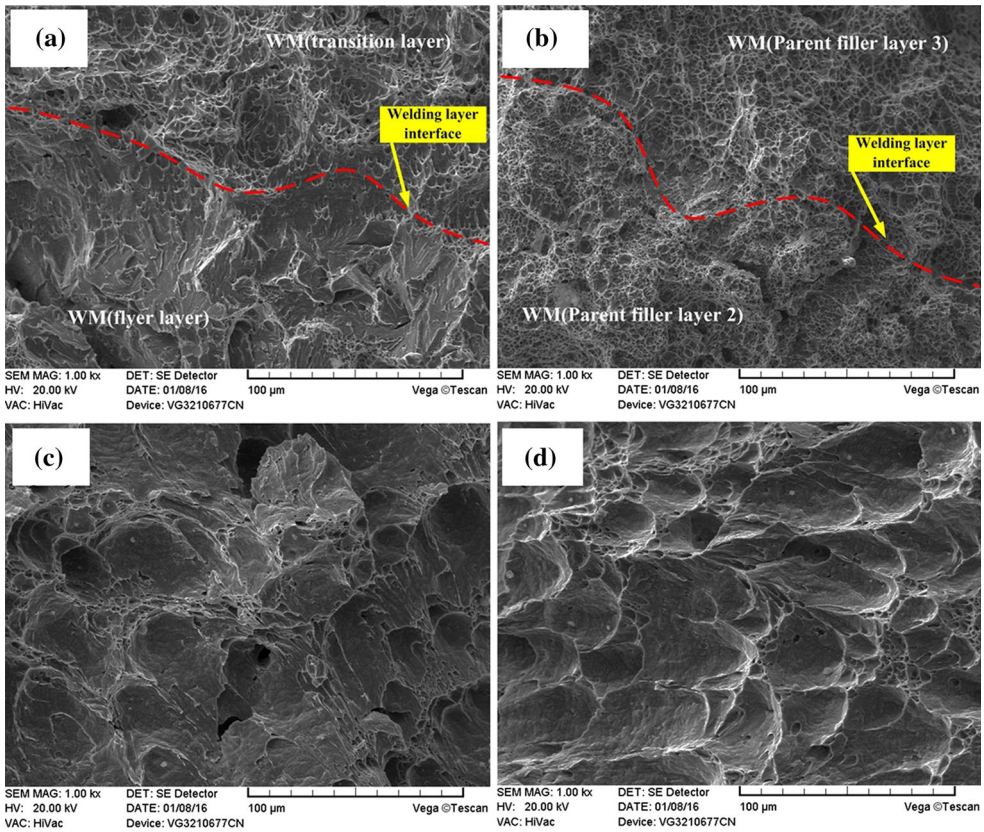

Fig. 11 Fracture morphology of impact samples: (a) WM in layer 1, (b) WM in layer 2, (c) HAZ in layer 1, and (d) HAZ in layer 2

higher hardness values corresponding to about 325 HV. Therefore, the flyer layer of the joint shows homogeneity of microhardness.

3.2.2 Tensile Test. Figure 8 shows the stress-time curves of tensile tests for the welded joint, indicating that the yield strength and tensile strength are 632 and 665 MPa respectively. Figure 9 shows the change of the maximum principal strain on the cross section of the joint during the tensile tests. Figure 9(a) demonstrates that the distribution of the maximum principal strain on the cross section of the joint is uniform in the elastic stage of the sample. As the tensile time increases, the sample reaches the yield point (position B on stress-time curves). The distributions of the maximum principal strain display obvious nonuniformity, and a significant strain concentration appears in the HAZ of the flyer weld (see Fig. 9B). Moreover, as the tensile time continues to increase, the strain keeps on increasing and gradually expands to the BM near the parent filler weld. When the sample reaches the tensile strength point (position C on stress-time curves), the BM near the parent filler weld undergoes an extremely localized deformation, which then increases throughout the entire BM (see Fig. 9D), leading to cracking and, finally, fracturing. A fracture of the tensile test specimen is marked by the rectangles in Fig. 9. The variation of maximum principal strain of positions 1–6 (p1–p6 in the inset in Fig. 8) on the cross section of the joint with time is also described in Fig. 8.

3.2.3 Impact Toughness. The impact strength values of the WM and the HAZ tested at −5 °C are presented in Fig. 10. Figure 10(a) shows that the WM of layer 3 exhibits the highest impact strength, and the average impact energy is 36.81 J. Compared to the WM of layer 2 with 31.08 J impact energy and the WM of layer 1 with impact energy of 25.03 J, the impact energy of the WM of layer 3 was 18 and 32% higher, respectively. Figure 11(b) shows the fracture morphology in the WM of layer 3, revealing that the mode of fracture in the weld metal of layer 3 was ductile with a dimpled structure in all the regions, including filler layer 3 (see upper part of Fig. 11b) and filler layer 2 (see lower part of Fig. 11b). Figure 11(a) shows the fracture morphology in the WM of layer 1, revealing fracture section including transition layer (upper part of Fig. 11a) and flyer (lower part of Fig. 11a). Figure 11(a) exhibits that the WM of transition layer shows a ductile mode of fracture, revealing a dimpled structure; however, the WM of flyer shows a typical mixed ductile-brittle fracture with a classical dimple appearance and quasi-cleavage appearance.

Figure 10(b) shows that the HAZ of layer 2 has the highest impact strength, and the average impact energy is 84.21 J, that is 40.95% higher than that of the HAZ of layer 1 and 8.19% higher than that of the HAZ of layer 3. The fracture section of the HAZ of layer 1 shows some big and shallow dimples and also some typical cleavage facets which reveal a character of mixed ductile-brittle fracture as shown in Fig. 11(c). In general, this brittle fracture can be attributed to the excessive ferrite and variations of Cr content in HAZ of 2205 (Ref 13, 14). Figure 10(d) shows the fracture morphology in the HAZ metal of layer 2, indicating that the HAZ of layer 2 shows excellent toughness in view of the fracture section, revealing big and deep dimples structure.

4. Conclusions

In this study, the butt joints of 2205/X65 bimetallic sheets were produced by multilayer and multi-pass gas tungsten arc welding and gas metal arc welding. Further, the inhomogeneity

of the properties of the welded joint was investigated. The following conclusions can be drawn from this study.

1. The microstructures of parent filler layers consisted of acicular ferrite, widmanstatten ferrite, and a small amount of blocky ferrite. The microstructures of the transition layer and flyer layer consisted of both austenite and ferrite structures; however, the transition layer of weld exhibited a higher volume fraction of austenite.
2. The results of hardness test showed that the hardness of flyer and the transition layers, and that of the 2205 was equivalent; however, the hardness decreased with the increase in the heat input for the parent filler layers.
3. Tensile test showed that the WM and HAZ of the flyer were prone to cause stress concentration, leading to failure of the joint.
4. Stratified impact test showed that the WM and HAZs of the filler layers exhibited a higher impact strength compared to the WM and HAZs of the flyer, and this was mainly due to the growth of ferrite grain size and decrease in austenite content in the WM and HAZ of the flyer.

Acknowledgments

The authors greatly acknowledge the support from the National High Technology Research and Development Program of China (Grant No. 2013AA031303HZ).

References

1. M. Acarer, B. Gülenç, and F. Findik, Investigation of Explosive Welding Parameters and Their Effects on Microhardness and Shear Strength, *Mater. Des.*, 2003, **24**, p 659–664
2. S.A.A. Akbari-Mousavi, L.M. Barrett, and S.T.S. Al-Hassani, Explosive Welding of Metal Plates, *J. Mater. Process. Technol.*, 2008, **202**, p 224–239
3. S.A.A. Akbari Mousavi and P. Farhadi Sartangi, Experimental Investigation of Explosive Welding of CP-Titanium/AISI, 304 Stainless Steel, *Mater. Des.*, 2009, **30**, p 459–468
4. Q.L. Chu, M. Zhang, J.H. Li, Q.Y. Fan, W.W. Xie, and Z.Y. Bi, Joining of CP-Ti/Q345 Sheets by Cu-Based Filler Metal and Effect on Interface, *J. Mater. Process. Technol.*, 2015, **225**, p 67–76
5. K. Devendranath Ramkumar, G. Thiruvengatam, S.P. Sudharsan Debidutta Mishra, N. Debidutta Mishra, N. Arivazhagan, and R. Sridhar, Characterization of Weld Strength and Impact Toughness in the Multi-Pass Welding of Super-Duplex Stainless Steel UNS 32750, *Mater. Des.*, 2014, **60**, p 125–135
6. F. Grignon, D. Benson, K.S. Vecchio, and M.A. Meyers, Explosive Welding of Aluminum to Aluminum: Analysis, Computations and Experiments, *Int. J. Impact Eng*, 2004, **30**, p 1333–1351
7. B. Gulenc, Investigation of Interface Properties and Weldability of Aluminum and Copper Plates by Explosive Welding Method, *Mater. Des.*, 2008, **29**, p 275–278
8. J.-B. Ju, W.S. Kim, and J. Jang, Variations in DBTT and CTOD Within Weld Heat-Affected Zone of API, X65 Pipeline Steel, *Mater. Sci. Eng. A*, 2012, **546**, p 258–262
9. R. Kacar and M. Acarer, An Investigation on the Explosive Cladding of 316 l Stainless Steel-Din-P355GH Steel, *J. Mater. Process. Technol.*, 2004, **152**, p 91–96
10. N. Kahraman and B. Gülenç, Microstructural and Mechanical Properties of Cu-Ti Plates Bonded through Explosive Welding Process, *J. Mater. Process. Technol.*, 2005, **169**, p 67–71
11. Y.C. Chen, L.W. Tsay, and S.L.I. Chan, Sulfide Stress Corrosion Cracking and Fatigue Crack Growth of Welded TMCP API, 5 l X65 Pipe-Line Steel, *Int. J. Fatigue*, 2001, **23**, p 103–113
12. M. Sadeghian, M. Shamanian, and A. Shafyei, Effect of Heat Input on Microstructure and Mechanical Properties of Dissimilar Joints between Super Duplex Stainless Steel and High Strength Low Alloy Steel, *Mater. Des.*, 2014, **60**, p 678–684
13. A.M. Torbati, R.M. Miranda, L. Quintino, and S. Williams, Welding Bimetal Pipes in Duplex Stainless Steel, *Int. J. Adv. Manuf. Technol.*, 2010, **53**, p 1039–1047
14. A.M. Torbati, R.M. Miranda, L. Quintino, S. Williams, and D. Yapp, Optimization Procedures for GMAW of Bimetal Pipes, *J. Mater. Process. Technol.*, 2011, **211**, p 1112–1116